Data-driven calculation of porous geometry-dependent permeability and fluid-induced wall shear stress within tissue engineering scaffolds

Matthew Bedding-Tyrrell, Nava Khatri, Perumal Nithiarasu, Bjornar Sandnes, Paul Egan & Feihu Zhao

View supplementary material ⬀

Published online: 03 Apr 2024.

Submit your article to this journal ⬀

Article views: 227

View related articles ⬀

View Crossmark data ⬀

🔓 OPEN ACCESS ⓜ Check for updates

Data-driven calculation of porous geometry-dependent permeability and fluid-induced wall shear stress within tissue engineering scaffolds

Matthew Bedding-Tyrrell[a,b], Nava Khatri[c], Perumal Nithiarasu[b,d], Bjornar Sandnes[e], Paul Egan[c] and Feihu Zhao[a,b]

[a]Department of Biomedical Engineering, Faculty of Science and Engineering, Swansea University, Swansea, UK; [b]Zienkiewicz Institute for Modelling, Data and AI, Swansea University, Swansea, UK; [c]Department of Mechanical Engineering, Texas Tech University, Lubbock, TX, USA; [d]Department of Civil Engineering, Faculty of Science and Engineering, Swansea University, Swansea, UK; [e]Complex Flow Lab, Department of Chemical Engineering, Faculty of Science and Engineering, Swansea University, Swansea, UK

ABSTRACT

It is commonly known that mechanical stimulation, for example, wall shear stress (WSS), can affect cellular behaviours. In vitro experiments have been performed by applying fluid-induced WSS to investigate the cell physiology and pathology. Porous scaffolds are used in these experiments for housing and facilitating the micro-physical/chemical environment on cells during 3-dimensional (3D) cell culturing. It is known that scaffold porous geometries influence scaffold permeability and internal WSS. Computational simulations are commonly employed to determine the WSS; however, these simulations can be computationally expensive and may not be readily accessible to everyone due to a knowledge gap. To address this limitation, this study proposes an empirical equation for calculating the scaffold permeability based on the Kozeny-Carman equation. The new equation considers the porous geometric features, providing an accurate estimation of the scaffold permeability. Furthermore, the study introduces a new correlation between WSS and permeability, aiming to establish an efficient and precise estimation of internal WSS. This correlation enables efficient estimation of the WSS within porous scaffolds without relying on computationally demanding simulations. Therefore, the output from this study can negate the issues of using computational simulation for determining scaffold permeability and internal WSS under perfusion flow by providing empirical equations.

1. Introduction

Porous scaffolds play an important part in tissue engineering experiments in vitro. They are used for housing the cells and facilitating the application of micro-physical/chemical

---

environment to cells during 3-dimensional (3D) cell culturing. The scaffolds have porous structures which can affect the micro-mechanical environment that the cells experience within a bioreactor (e.g. based on perfusion flow) (Pires et al. 2022). Therefore, the ability to tune the micro-mechanical environment for cells can be achieved via scaffold porous geometric design. The internal pressure and shear forces are stimuli for these cells and instigate cell differentiation and cell seeding (Castro et al. 2019). For example, a wall shear stress (WSS) between 0.1 and 10 mPa can stimulate mesenchymal stromal cells differentiating towards osteogenic lineage for bone tissue engineering in vitro (Melke et al. 2018).

Permeability is the measure of how well a scaffold can conduct and direct the flow of fluid as well as nutrient delivery throughout the scaffold (Dong and Zhao 2021). Tissue regeneration within a scaffold during cell culture processes is dependent on how well nutrients can permeate through the scaffold structure (Castro et al. 2019). A higher permeability can enhance nutrient diffusion through the scaffolds. However, the necessary corollary of high permeability is less structural material. The optimal permeability is therefore the highest permeability achievable whilst keeping the scaffold mechanically stable.

Scaffold permeability is dependent on architectural properties. Higher porosity will usually result in a higher permeability. However, a previous study found that the Schwarz P structures can have a decreased permeability with an increased porosity (Dong and Zhao 2021). Scaffold permeability also affects the WSS on cells within a scaffold according to previous findings (Ahmed et al. 2023; Vossenberg et al. 2009). As with permeability, WSS is also affected by variations in porous geometries (Ahmed et al. 2023; Vossenberg et al. 2009). Increases in pore size have been shown to cause oscillating variations in shear stress (Ouyang et al. 2019). A higher porosity has been shown, in the gyroid TPMS (triply periodic minimal surface) and a regular lattice structure, to give lower values for WSS (Ali and Sen 2017). For in vitro mechanobiological studies, the calculation of the WSS within scaffolds is necessary for assessing the cell responses under specific WSS. To facilitate fast and easy calculation of WSS within a scaffold, power-law functions that link WSS with permeability have been determined in previous studies (Ahmed et al. 2023). However, to do this, scaffold permeability needs to be determined first.

Another reason the architectural properties must be considered is that low interconnectivity between the pores in a structure will lead to a fast rate of pore occlusion (Abbasi et al. 2020). Pore occlusion reduces the ability of nutrients to permeate throughout the whole scaffold. To calculate the scaffold permeability, Darcy's law (Equation 1) is commonly used:

$$k = -\frac{Q \cdot \mu \cdot L}{A \cdot \Delta P} \tag{1}$$

where, Q is the flow rate, μ is the dynamic viscosity, L is the total length of the scaffold, A is the cross-sectional area and ΔP is the pressure change over the scaffold geometry.

To use Darcy's law for calculating the permeability of porous structure, the parameters (in Equation 1) need to be determined first. To determine the parameter (such as ΔP in Equation 1), it needs to be based on either experiment or simulation, which are costly in terms of time and finance, particularly for scaffolds with complex structures. Therefore, accurate and fast estimations of permeability based on geometric properties are highly valued. These accurate estimations are especially valuable for CFD models based upon micro-Computed Tomography (CT) images as the irregularity and complexity of the models lead to high computational costs. A more convenient way to estimate permeability is by

the Kozeny-Carman equation (Equation 2) (Latief and Fauzi 2012):

$$k = \left(\frac{1}{C_k}\right) \cdot \left(\frac{\varphi^3}{S_A{}^2}\right) \quad (2)$$

where, C_k is the empirical Kozeny constant, φ is porosity and S_A is the specific surface area.

One of the main limitations of the Kozeny-Carman equation is that C_k is highly dependent on pore geometry, and it is not currently possible to determine C_k without experimental or simulation results. For example, the Kozeny constant for a micro-CT-based model was determined both computationally and experimentally (Truscello et al. 2012). The results indicated a linear relationship between permeability and the ratio $\varphi^3/S_A{}^2$. It was found that more complex geometries had a non-linear relationship (Rahbari et al. 2017). The Kozeny-Carman constant of more complex geometries was shown to be fit by a second-order polynomial of porosity (Rahbari et al. 2017). TPMS are some of these complex geometries and have gained significant attention in tissue engineering scaffolds for several advantages, such as a high surface area to volume ratio, less stress concentration, and high permeability in comparison to regular lattice structures (Lu et al. 2020). These factors aid in better cell adhesion, migration, and proliferation (Murphy, Haugh, and O'Brien 2010). It was found that a second-order polynomial of the Napierian logarithm fits the Kozeny-Carman constant of TPMS geometries with a high accuracy (Zhang et al. 2020). The limitation was that a high number of simulations at different porosities of a single geometry must be completed to determine this relationship.

To address these limitations, in this study, it was hypothesised that an updated Kozeny-Carman equation for TPMS scaffolds could provide a more accurate prediction of the scaffold permeability, and thus WSS, using an empirical function. To test this hypothesis, the data-driven approach was used based on the permeability and WSS generated from the CFD model, which was calibrated and validated by fluidic experimental measurement. The output from this study will enable the fast estimation of the WSS and permeability of the TPMS scaffolds. Also, it is expected to facilitate scaffold porous geometry determination/design for 3D in vitro mechanobiological experiments.

2. Materials and methods

2.1. Scaffold geometric design

TPMS exhibit intriguing topological features and their interconnected porous network has led to them being used in tissue engineering. The solid structures, which are generated based on the surfaces, can take the form of one of two different lattices: a ligament-based (or skeletal) lattice and a sheet-based lattice (Abou-Ali, Lee, and Abu Al-Rub 2022). In a ligament-based lattice, the surface splits a volume into two parts. One of these parts is solidified and makes up the lattice. In a sheet-based lattice, two different surface topological equations are used and the gap between these two surfaces is then solidified. That solidified gap is used to make up the lattice. In this study, the ligament-based lattices and the TPMS lattices were used (e.g. as shown in Figures 1(a and b)).

The level-set approximation equations, based on trigonometric functions, were used to define the TPMSs to a high level of precision (Gandy et al. 2001). The gyroid and FKS surfaces
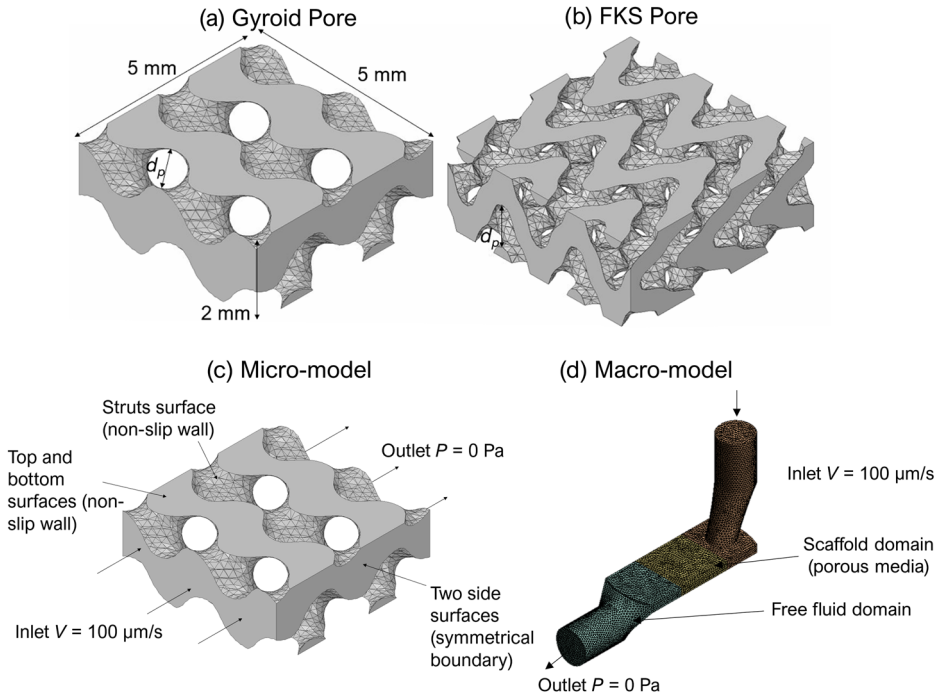
Figure 1. Geometric examples of (a) gyroid pore and (b) FKS pore; boundary conditions for (c) micro-model and (d) macro-model.

are described by the following equations respectively (Zou et al. 2022):

$$\Phi_G = cos(x)sin(y) + cos(y)sin(z) + cos(z)sin(x) - C \tag{3}$$

$$\Phi_{FKS} = cos(2x)sin(y)cos(z) + cos(x)cos(2y)sin(z) + sin(x)cos(y)cos(2z) - C \tag{4}$$

where C is the level-set constant and the surface of the structures is determined when $\Phi = 0$. When $-1 < C < 1$, C controls the pore morphology and therefore can be altered to change pore size and porosity (Lu et al. 2022).

In the Equations (3) and (4), level-set approximations equations were controlled by both the trigonometric functions and the level-set constant. Using the level-set equation, it could be determined whether a specified coordinate was on one side of the surface or on the other. This was determined by whether the sum of the trigonometric functions was greater or less than the level-set constant C. As the value of the level-set constant was altered, the number of coordinates on each side of the surface changed. This showed a direct relationship between the porosity of a TPMS scaffold and the level-set constant C. This relationship has already been determined for the gyroid surface (Equation 5) by Walker et al. (2017). Similarly, the pore size could be altered by changing the level-set constant. This relationship has also been identified for the gyroid surface (Equation 6) by Walker et al. (2017):

$$C = 0.7864\varphi^3 - 1.1798\varphi^2 - 2.5259\varphi + 1.4597 \tag{5}$$

$$d_p = -11.7311C^5 - 0.1307C^4 - 1.7987C^3 + 0.2070C^2 - 186.9928C + 433.0114 \tag{6}$$

where φ is the porosity, C is the level-set constant and d_p is the pore size.

Using these two relationships, TPMS scaffolds could be designed with both pore size and porosity as geometric factors in a MATLAB application – MSLattice (Al-Ketan and Abu Al-Rub 2021). In our study, the scaffolds with gyroid-shape struts (in Figure 1(a)) had porosities ranging from 50-90% and pore sizes from 600 to 1000 μm (Al-Ketan and Abu Al-Rub 2021), with overall dimensions of 12 × 12 × 2 mm. Using a similar method to Walker et al. (2017), pore size-constant and porosity-constant relationships were determined for the FKS surface (Figure 1(b)) as shown in Equations (7) and (8):

$$C = 0.7541\varphi^3 - 1.1294\varphi^2 - 1.5154\varphi + 0.9459 \tag{7}$$

$$d_p = 0.0835C^2 - 215.2690C + 216.4987 \tag{8}$$

Scaffolds of the FKS surface for dimensions 12 × 12 × 2 mm were also designed, and their porosity and pore size ranges were the same as the gyroid-shape struts.

2.2. Scaffolds manufacturing & experimental fluid measurement

The scaffolds were fabricated using an Envision One cDLM printer (EnvisionTEC, USA) with E-Shell Type 600 resin material (EnvisionTec, Dearborn, MI, USA). The Envision One printing system uses digital light processing with a native 93 μm xy-resolution, z-resolution from 50 to 150 μm, a 385 nm wavelength ultraviolet light-emitting diode (UV-LED) light source, and 180 by 101 by 175 mm build envelope. Prints were fabricated using a 50 μm layer thickness and 0.7 mm support tip thickness. Support size and build direction were systematically altered in multiple batches and visually inspected for quality and printability to determine a favourable printing configuration. The support material is provided on the bottom part of the sample, with the sample oriented in the upright position. Samples were printed at ambient temperature, with 17,500 ms initial burn-in time, 1000 ms waiting time before exposure, 300 μm separation velocity per second, and 5000 ms per layer exposure time. Prints were imported as STL files to Envision One Rapid Prototype software (EnvisionTec, v1.23.4820). After printing, lattices were removed from the build plate with a metal spatula. The support material was removed from the bottom of the lattices using a blade. The excess resin was removed using an isopropyl alcohol bath. Lattices were then placed in a PCA 2000 ultraviolet curing chamber (EnvisionTec) during post-processing for one hour. After test printing, it was found that the scaffolds with a porosity higher than 70% for the Gyroid and porosity higher than 60% for the FKS geometries have low manufacturability (e.g. imperfect/broken struts) for the Envision One cDLM printer. Among the designed scaffold geometries, the gyroid scaffold with porosity of 50% and pore size of 1000μm has the highest manufacturability, which resulted in the struts with clear gyroid shape as shown in the zoomed-in image of Figure 2(b). Based on visual inspection, we demonstrate the high printing quality of the scaffold used in the experiments in Figure 2(b). Therefore, the scaffold (porosity = 50%, pore size = 1000μm) was chosen to be used in a fluidic experiment for validating the CFD model mesh strategy.

In order to measure the fluidic pressure drop due to the scaffold, a millifluidic device was manufactured using a stereolithography (SLA) 3D printer, Flashforge Foto 8.9 (Flashforge, China). This method of 3D printing was used to limit micro-porosities throughout the device causing leak-off which would affect the flow rate and pressure results. In order to maintain high watertightness, grooves were designed to fit an 'O-ring' around the top part
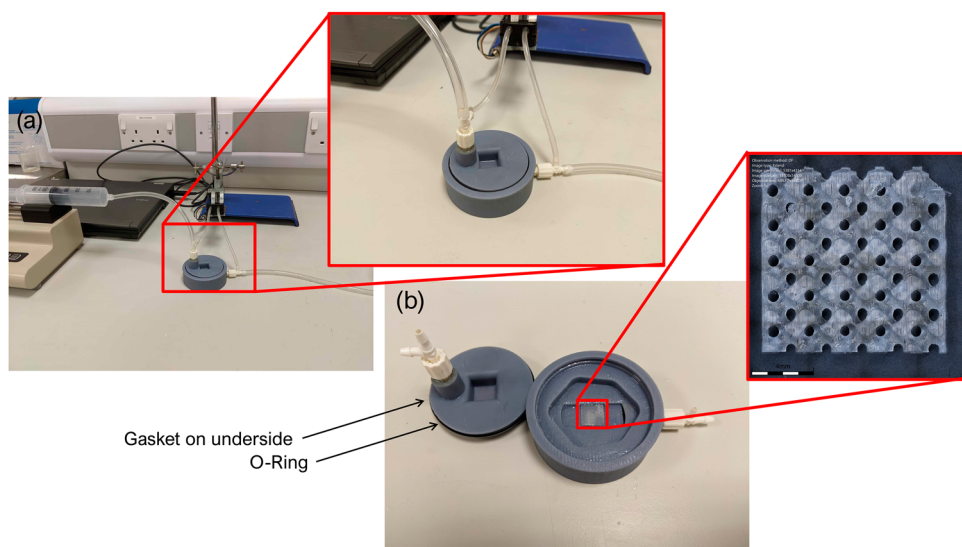
Figure 2. (a) Experimental setup for measuring the fluid pressure drop over the millifluidic device and (b) disassembled millifluidic device with expanded view of scaffold in place (scale bar = 4 mm).

of the device, shown in Figure 2(b). Additionally, a silicone gasket was placed in between the two parts of the device. Although the gasket and the 'O-ring' ensure a leak-free system, visual checks were carried out to guarantee direct perfusion without leaks. The scaffold was placed inside a tight-fitting flow channel in the millifluidic device as shown in Figure 2(b) and the pressure change across the lattice was recorded. The Sensirion SDP800-125 Pa (Sensirion AG, Switzerland) was used as the pressure sensor for the experiment. The sensor was connected to the millifluidic device at the inlet and outlet as shown in Figure 2. The sensing lines were cut to a length to be tight and to keep the sensor above the inlet, thus allowing high perfusion through the device. A syringe pump was connected to the device and was set to apply a 3 mL/min flow rate of water for a total 10 mL over each scaffold. Before each measurement, the syringe was expunged to reduce the risk of air bubbles in the fluid. The presence of air bubbles would have had an adverse effect on the flow rate through the millifluidic device, thus affecting the pressure difference. The Sensirion Evaluation Kit was connected to the pressure sensor and the USB RS485 Sensor Viewer software was used to record and export the pressure differential data. Using the exported data from the USB RS485 Sensor Viewer software (Sensirion AG, Switzerland), peaks of pressure difference were observed. Then the average pressure difference was recorded during the time period, which covered 2 full peaks for each scaffold.

2.3. Multiscale CFD model

To obtain the scaffold permeability and resultant WSS within scaffolds, the CFD model was run alongside the experimental setup. Using Computer-Aided Design (CAD) data for the 3D-printed millifluidic device, a geometric inverse was produced to establish the fluid domain (Figure 1(d)). Due to the complexity of the scaffolds, a direct CFD model would have incurred a high computational cost. To lower the computational cost, a multiscale

approach previously developed by Zhao et al. (Zhao et al. 2019) was used instead. The multiscale approach split a full-scale CFD model into two distinct simulations (Figure 1(c and d)). The first CFD simulation determined the permeability and WSS of the scaffold based on a micro-model geometry. This micro-CFD model calculated the pressure drop over the scaffold, which was used for calculating the permeability according to Darcy's law (Equation 1). The second simulation used a macro-model geometry, which represented the whole chamber of fluidic device, to determine the overall pressure drop. In this macro-model, the whole scaffold was modelled by homogeneous porous media using the calculated permeability from the micro-model. The pressure drop from the inlet to the outlet was compared to the experimental measurement in order to validate the CFD model in terms of mesh strategy and boundary conditions. The macro-model in this multiscale approach was the fluid domain found from the millifluidic device's CAD data and the micro-model was a 5 × 5x2 mm section of the geometric inverse of each of the scaffold geometries (Figure 1(a and b)). The first simulation in the multiscale approach was designed with a velocity of 1 mm/s inlet and a zero-pressure outlet, with water as a medium to computationally replicate the experimental setup. The fluid region was defined as a free fluid and incompressible Newtonian laminar flow, which follows the Navier-Stokes equations. A mesh-dependent study was completed on the most computationally expensive gyroid geometry (i.e. 90% porosity, 600 μm pore size), and it was determined that a mesh cell number of 1,000,000 was optimal based on the accuracy of the result and computational cost. The CFD models were completed using a finite volume method (FVM) using ANSYS CFX (ANSYS Inc., PA, USA). Pressure-velocity coupling is used in CFX and is implemented using the Rhie-Chow algorithm. The convergence criteria of root-mean-square residual of the mass and momentum were set as $< 10^{-4}$. All the simulations were run on the computer with 128GB RAM and an Intel i7 12700 CPU (12 cores).

2.4. Data analysis

To determine the relationship between the geometric properties-permeability and WSS-permeability, regression analysis was performed on both datasets, which contained permeability and WSS under different scaffold porous geometries generated in Section 2.1. The FKS and gyroid structures both were made up of non-symmetric pore units. Although a recent study has sought to find a uniform power-law relationship between WSS and permeability for all non-symmetric shapes of pore units, the prediction accuracy still varied among different shapes of pore units (Ahmed et al. 2023). For this reason, the regression analysis was not only conducted on the combined results of both structures but also on the individual structures' results using Matlab (MathWorks Ltd, MA, USA).

3. Results

3.1. Experimental validation of the CFD model

From the fluidic experimental measurement (applied flow rate = 3 mL/min), the pressure drop (from inlet to outlet of a fluidic device) was 2.76 Pa. After adjusting the mesh strategy, the CFD simulated pressure drop was 2.51 Pa. This showed that the CFD domain meshed with 1,000,000 elements has a good accuracy. Then we applied this mesh strategy

(i.e. meshing the CFD domain with approximately 1,000,000 cells) to the simulations of all scaffolds, which were designed in section 2.1.

3.2. Updated Kozeny-Carman equation for permeability calculation

The range of permeabilities for the FKS and gyroid scaffolds for all porosities and pore sizes was of the order of 10^{-8} m^2; and the WSS range over applied velocity results was of an order of magnitude of 10^1 Pa, which was similar to the results of (Ahmed et al. 2023). The gyroid architecture showed that both porosity and pore size are important variables in altering permeability. Increases in both porosity and pore size lead to increases in permeability. Increases in pore size lead to decreases in WSS and increases in porosity lead to minor decreases in WSS. The permeability trend matched the FKS architecture with increases in porosity and pore size leading to clear increases in permeability. The previous finding by Ahmed et al (Ahmed et al. 2023) showed that an increase in pore size could lead to decreases in WSS was also observed in our study. In contrast to the gyroid results, when analysing the influence of the porosity on the FKS results, the higher WSS values occurred at 60% and 70% porosity with the lower values of WSS occurring at the periphery porosity values (50% and 80%).

As indicated by Zhang et al. (Zhang et al. 2020), the relationship between permeability and the ratio φ^3/S_A^2 for TPMS structures is not linear. This was also shown by the simulation results for both the gyroid and FKS architectures. The results indicated that an altered Kozeny-Carman equation could fit the results more accurately, where the exponent of porosity was replaced with a value of n which was a function of porosity. The relationship between the exponent and porosity is shown in Figure 3. Instead of a second-order polynomial relationship with porosity, a negative exponential relationship was for the FKS architecture, and a power law relationship was for the gyroid architecture. These relationships were given in Equation (9) (for FKS architecture) and Equation (10) (for gyroid architecture):

$$n(\varphi) = -8.97 \times 10^{-6} e^{16.3\varphi} + 10.32 e^{-2.259\varphi} \tag{9}$$

$$n(\varphi) = -46.75\varphi^{8.405} + 2.779. \tag{10}$$

Figures 4(a and b) showed the multi-variable relationships (2D surfaces), which were described by Equation (11):

$$k = \left(\frac{\varphi^n}{S_A^2}\right) \tag{11}$$

where, n is dependent on porosity (φ), and is determined as shown in supplementary material – Supplementary Figure 1.

The data points shown in Figure 4 were the permeability results from CFD simulations, plotted against the porosity of the porous scaffolds and their specific surface area. A clear similarity between the updated Kozeny-Carman equation and the CFD permeability results could be observed.

Using the updated Kozeny-Carman model, with the relationships given in Equations (9) and (10), the estimated permeability could be used to calculate the pressure drop over the scaffolds within the millifluidic device. For the highest quality scaffold (i.e. gyroid struts,
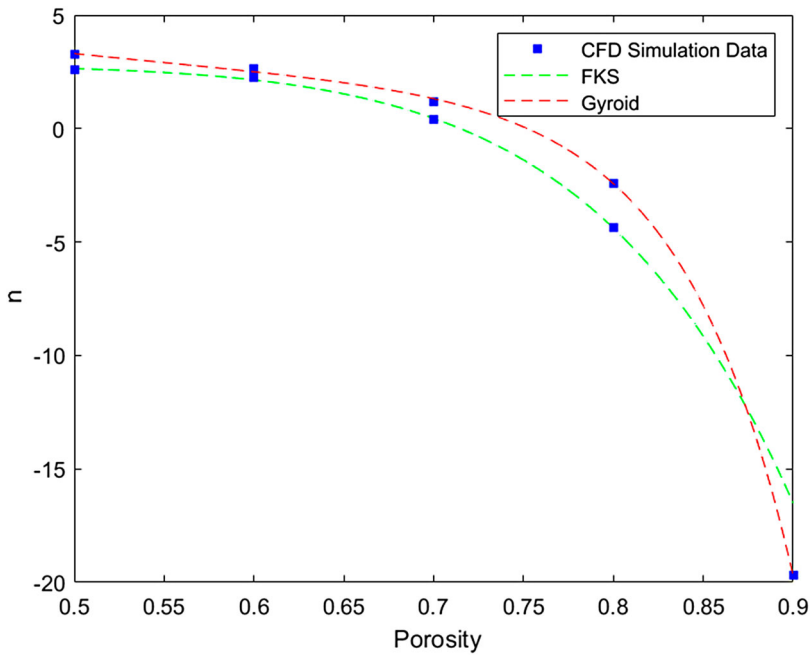
Figure 3. Relationships between exponent n and porosity for Equations (9) and (10).
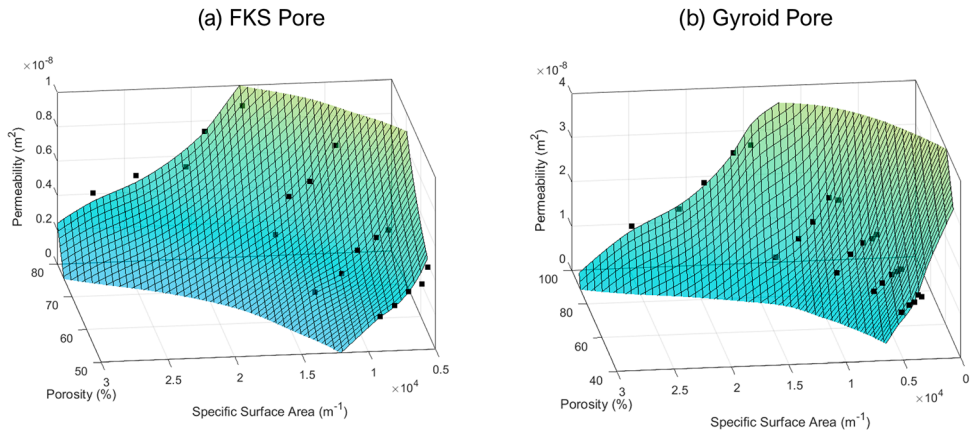
Figure 4. Permeability results calculated by updated Kozeny-Carman equation (surface) and CFD simulation (dots) for the scaffolds that have (a) FKS pores and (b) gyroid pores with different porosities and specific surface areas.

porosity $= 50\%$, and pore size $= 1000\,\mu m$), the estimated permeability was $1.12 \times 10^{-8}\,m^2$ compared to the simulated $1.03 \times 10^{-8}\,m^2$. This estimated permeability was then used in the multiscale model to give the estimated pressure drop over the millifluidic device. This gave a pressure drop of 2.11 Pa, compared to the experimental result of 2.76 Pa.

Figures 5(a and b) indicate the percentage difference of permeability calculated by the updated Kozeny-Carman equation and CFD simulation. The gyroid data shows an average percentage difference of 11.69%. The FKS geometry has an average percentage difference
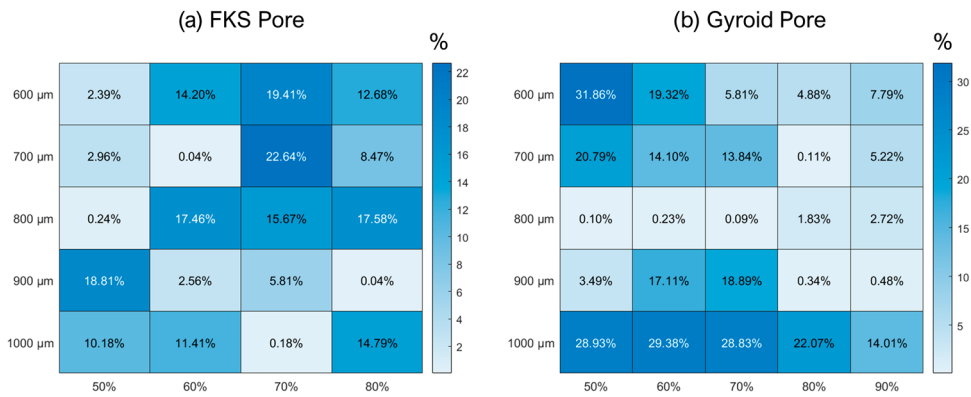
Figure 5. Error maps indicating the percentage difference of the permeability calculated by updated Kozeny-Carman equation and CFD simulation for (a) FKS pores and (b) gyroid pores, with different pore sizes (vertical axis) and porosities (horizontal axis).

of 9.88%. The colour bar indicates the percentage difference where a darker blue shows a larger percentage difference and a lighter blue indicates a lower percentage difference between the updated Kozeny-Carman equation and the CFD results. There was no clear common trend in the FKS pore data, rather there were regions of high or low percentage differences. A clear higher percentage difference region occurred at 70–80% porosity and between 600 and 800 μm; whilst a lower percentage difference region occurred at 50% porosity between 600 and 800 μm. These two main regions indicated that lower porosities tended to have a stronger fit with the updated Kozeny-Carman model. For instance, for the FKS architecture, an average difference of only 6.92% was found for the geometries with 50% porosity. In the case of the gyroid architecture, an inverse trend could be seen. Higher porosity showed a much better fit to the updated model. Decreases in percentage difference could be seen with an increasing porosity between 50% and 80%. There were also more significant regions in the gyroid data, the clearest one being 800 μm for all porosities having a percentage difference of 0.99%. The scaffolds with porosities of 80%–90% and pore size of 600 μm–900 μm had a low difference in terms of permeability by updated Kozeny-Carman model and CFD simulation, whilst porosities of 50%–70% and pore sizes of 900 μm–1000 μm were in a higher difference region with an average of 21.10% (Figure 5(b)).

3.3. WSS – permeability correlation

To facilitate the efficient calculation of WSS within tissue engineering scaffolds for mechanobiology applications, the correlation between WSS and permeability was derived in this study. Since the average WSS (τ) within the scaffolds is proportional to the applied fluid velocity (V) (Ahmed et al. 2023), we introduced a parameter $\gamma = \tau / V$. Figure 6 exhibited a derived power law relationship between the permeability and WSS results. The relationship was derived from four different equations, which were: Darcy's Law (1), Kozeny-Carman Equation (2), a relationship between pressure drop (ΔP) and WSS in Equation (12) and the equation for hydraulic diameter (D_H) based on scaffold porosity (φ) and specific surface area S_A in Equation (13) (Darcy 1856; Ibragimov 2011; Li, Li, and Yu 2022). This derived
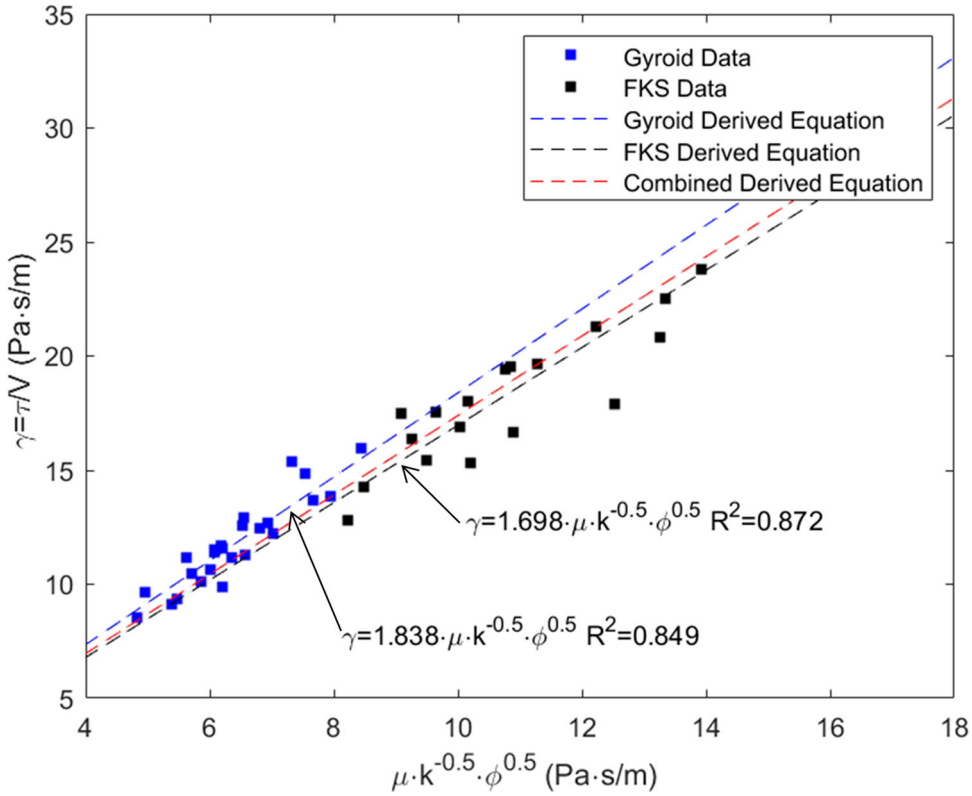
Figure 6. Functions for calculating WSS (τ) using permeability (κ), dynamic viscosity (μ), velocity (V) and porosity (φ) obtained by linear regression analysis.

relationship was in Equation (14) below:

$$\tau = \frac{\Delta p \cdot D_H}{4L} \tag{12}$$

$$D_H = \frac{4\varphi}{S_A} \tag{13}$$

$$\gamma = \frac{\tau}{V} = C_S \cdot \mu \cdot \sqrt{\frac{\varphi}{k}} \tag{14}$$

where C_S is the constant determined by regression analysis, e.g. $C_S = 1.698$ and 1.838 for the scaffolds with FKS architecture ($R^2 = 0.849$) and gyroid architecture ($R^2 = 0.872$), respectively. If combine all scaffolds together, we had an overall $C_S = 1.74$ with $R^2 = 0.928$ as shown in Figure 6.

4. Discussion

In this study, for validating the CFD model, the pressure drop results between the experiment and simulation of a manufactured scaffold with the highest quality (i.e. gyroid struts, pore size = 1000μm, porosity = 50%) were highly aligned. Therefore, it could be deduced that if additional scaffolds were manufactured to this high quality, then it would be likely to

produce similarly comparable results. Using these simulation results, an updated Kozeny-Carman equation for scaffold permeability calculation was developed, based on specific surface area, porosity, and a porosity-dependent exponent. A new relationship between WSS and permeability was also determined, based on fluid dynamic viscosity, fluid velocity, and scaffold porosity.

The experimental data shows that 3D printing TPMS structures with high porosities (larger than 70%) and low pore sizes (smaller than 800 μm) is currently not feasible with the Envision One cDLM printer. However, that printer can accurately produce the gyroid structure with pore sizes of 1000 μm and larger, with porosities of 50% and 60%. The low resolution of the scaffold struts with small pores and high porosity was also reflected in the comparison between fluidic measurement and refined CFD simulation (see supplementary material). It is recommended that for future studies, these more difficult-to-manufacture structures should use an alternative method of additive manufacturing, such as high-end selective laser sintering or directed energy deposition-arc machines. Melt electro-writing machines have also been used recently to produce microporous scaffolds specifically for tissue engineering (Loewner et al. 2022).

The simulation results show that there was a clear negative exponential relationship between the exponent n and porosity in Kozeny-Carman equation for the gyroid architecture and a power law relationship for the FKS architecture. In this study, we improved the original Kozeny-Carman equation by providing an alternative varying exponent for predicting the porous structure permeability, which was beyond the capability of the original Kozeny-Carman equation. For example, it was found that the FKS structures below a porosity of 40% would be mathematically similar to the original Kozeny-Carman equation, however with an exponent (n) value of 2.77 instead of 3. Whilst the exponent (n) for the gyroid structures continued to increase as porosity decreased below 50%, to a maximum of 10.3.

An alternative Kozeny-Carman equation was also sought as Equation (15):

$$k = C_1 \cdot \left(\frac{\varphi^3}{(1 - \varphi)^2 \cdot S_A{}^2} \right) + C_2 \tag{15}$$

where C_1 and C_2 are obtained through regression analysis from the CFD permeability results and geometries of individual specific surface areas (S_A).

The average percentage difference of permeability between the CFD results and the alternative Kozeny-Carman equation (Equation 15) for the gyroid and FKS architectures were 7.6% and 11.94%, respectively (Supplementary Figures 2–3 in supplementary material). Equation (15) overall had a lower percentage difference for the gyroid architecture compared to our updated model (Equation 11). However, for both the gyroid and FKS architectures, the updated model (Equation 11) had significantly more results of the percentage difference below 1%. Ten results have percentage differences below 1% for the updated model (Equation 11), compared to only 2 for this model (Equation 15). Additionally, the highest percentage difference of the permeability by Equation (15) and CFD simulation was 45.44%, which happened on the scaffold with FKS pore shape, porosity = 60% and pore size = 600 μm (see Supplementary Figure 3 in supplementary material). Equation (15) had the advantages of (i) only using 2 constant values rather than 3 and 4 for the FKS and gyroid respectively; (ii) mathematically simpler to use. Nevertheless, the high quantity of < 1% difference values for the updated model (Equation 11) indicated its superiority over this more

commonly used Kozeny-Carman model Equation (15) (see the fitting and errors in Figures 4–5 vs Supplementary Figures 2–3).

The previous relationship between WSS and permeability was based on a power law relationship, where there were two fitted constants – a coefficient and an exponent (Ahmed et al. 2023). We tested the power law relationship reported by Ahmed et al. (2023) by fitting it to our CFD results (see supplementary material – Supplementary Figure 4). There were two clear anomalous data points in the gyroid data, which caused a low R^2 value. Also, compared to the results from Equation (14) in this study, a higher R^2 value was found in Equation (14) than that on the equation in (Ahmed et al. 2023) (Figure 6 vs. Supplementary Figure 4), meaning our Equation (14) was more accurate for WSS calculation according to known permeability. Moreover, the updated relationship (Equation 14) was easier to derive as it only required 1 constant rather than 2, and could also be used for alternative mediums with different dynamic viscosities. This new relationship gave dimensionless constant C_S values of 1.698 and 1.838 for FKS and gyroid shapes respectively (or 1.74 if the constant is geometrically standardised). Future studies need to be completed on comprehensive sensitivity analysis of constant C_S influenced by scaffold architectures, such as other TPMS scaffolds – namely the Schwarz P, Double Gyroid, Diamond, or FRD.

5. Conclusion

One of the biggest challenges in tissue engineering scaffold design is to design scaffolds to specified properties (e.g. permeability) and internal mechanical environment (e.g. WSS) for 3D mechanobiological applications. This study has provided accurate and efficient tools to improve intuitive TPMS scaffold design and/or characterisation of both parameters (permeability and WSS), specifically:

- an updated Kozeny-Carman equation for scaffold permeability calculation, considering the porosity and specific surface area;
- a new correlation between WSS and permeability for accurate and efficient estimation of internal WSS.

Disclosure statement

No potential conflict of interest was reported by the authors.

Funding

References

Abbasi, Naghmeh, Stephen Hamlet, Robert M. Love, and Nam Trung Nguyen. 2020. "Porous Scaffolds for Bone Regeneration." *Journal of Science: Advanced Materials and Devices* 5 (1): 1–9. https://doi.org/10.1016/j.jsamd.2020.01.007.

Abou-Ali, Aliaa M., Dong Wook Lee, and Rashid K. Abu Al-Rub. 2022. "On the Effect of Lattice Topology on Mechanical Properties of SLS Additively Manufactured Sheet-, Ligament-, and Strut-Based Polymeric Metamaterials." *Polymers* 14 (21). https://doi.org/10.3390/polym14214583.

Ahmed, Husham, Matthew Bedding-Tyrrell, Davide Deganello, Zhidao Xia, Yi Xiong, and Feihu Zhao. 2023. "Efficient Calculation of Fluid-Induced Wall Shear Stress Within Tissue Engineering Scaffolds by an Empirical Model." *Medicine in Novel Technology and Devices* 18 (June): 100223. https://doi.org/10.1016/j.medntd.2023.100223.

Al-Ketan, Oraib, and Rashid K. Abu Al-Rub. 2021. "MSLattice: A Free Software for Generating Uniform and Graded Lattices Based on Triply Periodic Minimal Surfaces." *Material Design and Processing Communications* 3 (6). https://doi.org/10.1002/mdp2.205.

Ali, Davar, and Sadri Sen. 2017. "Finite Element Analysis of Mechanical Behavior, Permeability and Fluid Induced Wall Shear Stress of High Porosity Scaffolds with Gyroid and Lattice-Based Architectures." *Journal of the Mechanical Behavior of Biomedical Materials* 75 (November): 262–270. https://doi.org/10.1016/j.jmbbm.2017.07.035.

Castro, A. P. G., T. Pires, J. E. Santos, B. P. Gouveia, and P. R. Fernandes. 2019. "Permeability Versus Design in TPMS Scaffolds." *Materials*. https://doi.org/10.3390/ma12081313.

Darcy, Henry. 1856. Les fontaines publiques de la ville de Dijon.

Dong, Zhifei, and Xin Zhao. 2021. "Application of TPMS Structure in Bone Regeneration." *Engineered Regeneration* 2 (January): 154–162. https://doi.org/10.1016/j.engreg.2021.09.004.

Gandy, Paul J.F., Sonny Bardhan, Alan L. Mackay, and Jacek Klinowski. 2001. "Nodal Surface Approximations to the P, G, D and I-WP Triply Periodic Minimal Surfaces." *Chemical Physics Letters* 336 (3-4): 187–195. https://doi.org/10.1016/S0009-2614(00)01418-4.

Ibragimov, M. H. 2011. "Channel Flow." *A-to-Z Guide to Thermodynamics, Heat and Mass Transfer, and Fluids Engineering*, August. https://doi.org/10.1615/ATOZ.C.CHANNEL_FLOW.

Latief, Fourier Dzar Eljabbar, and Umar Fauzi. 2012. "Kozeny–Carman and Empirical Formula for the Permeability of Computer Rock Models." *International Journal of Rock Mechanics and Mining Sciences* 50 (February): 117–123. doi:10.1016/j.ijrmms.2011.12.005.

Li, Wenguang, Weihong Li, and Zhibin Yu. 2022. "Heat Transfer Enhancement of Water-Cooled Triply Periodic Minimal Surface Heat Exchangers." *Applied Thermal Engineering* 217 (November). https://doi.org/10.1016/j.applthermaleng.2022.119198.

Loewner, Sebastian, Sebastian Heene, Timo Baroth, Henrik Heymann, Fabian Cholewa, Holger Blume, and Cornelia Blume. 2022. "Recent Advances in Melt Electro Writing for Tissue Engineering for 3D Printing of Microporous Scaffolds for Tissue Engineering." *Frontiers in Bioengineering and Biotechnology*. https://doi.org/10.3389/fbioe.2022.896719.

Lu, Yongtao, Liang Liang Cheng, Zhuoyue Yang, Junyan Li, and Hanxing Zhu. 2020. "Relationship Between the Morphological, Mechanical and Permeability Properties of Porous Bone Scaffolds and the Underlying Microstructure." *PLoS ONE* 15 (9 September): 1–19. https://doi.org/10.1371/journal.pone.0238471.

Lu, Chenxi, Yufeng Zhang, Muhammad Aziz, Pin Wen, Chi Zhang, Qiang Shen, and Fei Chen. 2022. "Mechanical Behaviors of Multidimensional Gradient Gyroid Structures Under Static and Dynamic Loading: A Numerical and Experimental Study." *Additive Manufacturing* 59 (November). https://doi.org/10.1016/j.addma.2022.103187.

Melke, J., F. Zhao, B. van Rietbergen, K. Ito, and S. Hofmann. 2018. "Localisation of Mineralised Tissue in a Complex Spinner Flask Environment Correlates with Predicted Wall Shear Stress Level Localisation." *European Cells and Materials* 36: 57–68. https://doi.org/10.22203/eCM.v036a05.

Murphy, Ciara M., Matthew G. Haugh, and Fergal J. O'Brien. 2010. "The Effect of Mean Pore Size on Cell Attachment, Proliferation and Migration in Collagen-Glycosaminoglycan Scaffolds for Bone Tissue Engineering." *Biomaterials* 31 (3): 461–466. https://doi.org/10.1016/j.biomaterials.2009.09.063.

Ouyang, Pengrong, Hui Dong, Xijing He, Xuan Cai, Yibin Wang, Jialiang Li, Haopeng Li, and Zhongmin Jin. 2019. "Hydromechanical Mechanism Behind the Effect of Pore Size of Porous Titanium Scaffolds on Osteoblast Response and Bone Ingrowth." *Materials & Design* 183 (December): 108151. https://doi.org/10.1016/j.matdes.2019.108151.

Pires, Tiago H.V., John W.C. Dunlop, André P.G. Castro, and Paulo R. Fernandes. 2022. "Wall Shear Stress Analysis and Optimization in Tissue Engineering TPMS Scaffolds." *Materials* 15 (20): 7375. https://doi.org/10.3390/ma15207375.

Rahbari, A., H. Montazerian, E. Davoodi, and S. Homayoonfar. 2017. "Computer Methods in Biomechanics and Biomedical Engineering Predicting Permeability of Regular Tissue Engineering

Scaffolds: Scaling Analysis of Pore Architecture, Scaffold Length, and Fluid Flow Rate Effects." *Computer Methods in BiomeChaniCs and BiomediCal Engineering* 20 (3): 231–241. https://doi.org/10.1080/10255842.2016.1215436.

Truscello, S., G. Kerckhofs, S. Van Bael, G. Pyka, J. Schrooten, and H. Van Oosterwyck. 2012. "Prediction of Permeability of Regular Scaffolds for Skeletal Tissue Engineering: A Combined Computational and Experimental Study." *Acta Biomaterialia* 8 (4): 1648–1658. https://doi.org/10.1016/j.actbio.2011.12.021.

Vossenberg, Petra, G. A. Higuera, G. Van Straten, C. A. Van Blitterswijk, and A. J. B. Van Boxtel. 2009. "Darcian Permeability Constant as Indicator for Shear Stresses in Regular Scaffold Systems for Tissue Engineering." *Biomechanics and Modeling in Mechanobiology* 8 (6): 499–507. https://doi.org/10.1007/s10237-009-0153-6.

Walker, Jason M, Emily Bodamer, Alex Kleinfehn, Yuanyuan Luo, Matthew Becker, and David Dean. 2017. "Design and Mechanical Characterization of Solid and Highly Porous 3D Printed Poly(Propylene Fumarate) Scaffolds." *Progress in Additive Manufacturing* 2 (1-2): 99–108. doi:10.1007/s40964-017-0021-3.

Zhang, Lei, Bo Song, Lei Yang, and Yusheng Shi. 2020. "Tailored Mechanical Response and Mass Transport Characteristic of Selective Laser Melted Porous Metallic Biomaterials for Bone Scaffolds." *Acta Biomaterialia* 112 (August): 298–315. https://doi.org/10.1016/j.actbio.2020.05.038.

Zhao, Feihu, Johanna Melke, Keita Ito, Bert Van Rietbergen, and Sandra Hofmann. 2019. "A Multiscale Computational Fluid Dynamics Approach to Simulate the Micro-Fluidic Environment Within a Tissue Engineering Scaffold with Highly Irregular Pore Geometry." *Biomechanics and Modeling in Mechanobiology* 18 (6): 1965–1977. https://doi.org/10.1007/s10237-019-01188-4.

Zou, Sijia, Yanru Mu, Bingchu Pan, Guangyong Li, Lei Shao, Jianke Du, and Yuan Jin. 2022. "Mechanical and Biological Properties of Enhanced Porous Scaffolds Based on Triply Periodic Minimal Surfaces." *Materials and Design* 219 (July). https://doi.org/10.1016/j.matdes.2022.110803.